

Supporting Information

A Free Standing Ru-TiC Nanowire Array/Carbon Textile Cathode with Enhanced Stability for Li-O₂ Batteries

Chenjuan Liu,^a Zhen Qiu,^b William R. Brant,^a Reza Younesi,^a Yue Ma,^c Kristina Edström,^a Torbjörn Gustafsson,^a and Jiefang Zhu^{*,a}

^a Ångström Advanced Battery Centre (ÅABC), Department of Chemistry - Ångström Laboratory, Uppsala University, Box 538, SE-75121, Uppsala, Sweden.

^b Department of Engineering Sciences, Solid State Physics, Uppsala University, Box 534, 75121 Uppsala, Sweden.

^c State Key Laboratory of Solidification Processing, Center for Nano Energy Materials, School of Materials Science and Engineering, Northwestern Polytechnical University, 710072 Xi'an China.

E-mail: jiefang.zhu@kemi.uu.se; Fax: +46 18 51 3548; Tel: +46 18 471 3722

To enhance the Li-O₂ battery performance and lifetime, understanding the electrochemical mechanism over cycling is critically important. Various advanced *in situ* and *in operando* characterization techniques have been developed during the recent years, providing indispensable insights for understanding the cell working mechanisms. Here we summarized and compared these advanced characterizations used in Li-O₂ batteries.

From Table S1, all these *in situ* and *operando* characterization techniques make unique contributions to the study of Li-O₂ batteries, and also have their technique limitations. Generally speaking, most of these techniques can only provide local (e.g., Raman, SEM, TEM) and/or surface (e.g., Raman, Surface-enhanced IR, XPS, SEM, AFM) information on the cathode. In addition, most of them cannot give quantitative information. Note these two limitations are somewhat related to each other. Only quantitative information on a bulk scale is representative, since the mixture cathode materials cannot guarantee homogeneity. Furthermore, most of them cannot give a real-time information (i.e., high time-resolution). Here, we must highlight DEMS and SR-PXD (used in this work). DEMS can track the gas evolution from the charge process of Li-O₂ batteries. Only one concern about DEMS is that these gas products may not originate from “their expected reactions” (e.g., O₂ does not have to be produced from the decomposition of Li₂O₂, and CO₂ could also be formed from side chemical reactions, instead of side electrochemical reactions). The “indirect” information from DEMS brings forth some challenges to the study of the electrochemical reaction during the charge process. SR-PXD can quantitatively track Li₂O₂ during both discharge and charge on a bulk scale and in a real-time (with time resolution about a few seconds). Of course, we could expect brilliant outcomes from the combination of SR-PXD and DEMS.

Table S1. State-of-the-art in situ and operando characterization techniques for Li-O₂ batteries

Technique	Sample preparation	Cell design	Quantification	Identify discharge products	Micro-structure	Time resolution	Limitation	Reference
Raman	Gold surface enhanced	Uncommon cell, Gold electrode	No/Difficult	Yes	No/Difficult	1 min	Difficult to apply to carbon electrode, low time resolution	1
Surface-enhanced IR	Gold surface enhanced	Uncommon cell, Gold electrode	No	No/Difficult	No	1 min	Peak overlapping, huge IR absorption by the electrolyte	2
DEMS	Regular preparation	Special cell setup	Yes, only gas phase	No	No	5-15 min	Only detect gas phase	3,4
XPS	Complex and difficult	Only solid-state Li-O ₂ cell (Uncommon cell)	No/difficult	No	No	15 min	Can only look at the very surface (1-2 nm), difficult to apply to regular cell.	5
SEM	Difficult	Tiny solid-state Li-O ₂ cell (Uncommon cell)	No	No	No/difficult	1-5 min	Only locally visualize morphology, Li ₂ O ₂ is sensitive to electron beam	6
TEM	Difficult	Uncommon cell	No	No/difficult	Yes	3-4 min	Local analysis, Li ₂ O ₂ is very sensitive to electron beam. Not be able to measure the true overpotential.	7
AFM	Complicated	Small electrodes	No	No	No/difficult	6.5 min	Local topology, difficult to apply to regular cell	8
XRD (in house)	Simple (regular preparation)	Complex cell set up	Yes/difficult	Yes	Yes/difficult	30 min	Low resolution	9,10
XRD (synchrotron) by others	Simple (regular preparation)	Complex cell set up	Yes/difficult	Yes	Yes	10s-5min	Difficult to get beam time	11-17
XRD (SR-PXD)	Simple (regular preparation)	Simple set up, common cell	Yes	Yes	Yes	10s	Difficult to get beam time	18 And this work

Table S2. The performance of TiC and other cathode materials

Sample	Preparation	Electrolyte	Anode	Cathode, Free-standing	Discharge current density (mA/g) ^a	Discharge Capacity (mAh/g)	Cycle Number ^b	Reference
TiC powder	Commercial	0.5 M LiClO ₄ in DMSO	LiFePO ₄	No (4% PTFE)	1 (mA/cm ²)	350	100	19
TiC powder	Commercial	0.5 M LiPF ₆ in TEGDME	LiFePO ₄	No (4% PTFE)	0.5 (mA/cm ²)	500	25	19
TiC-A powder	Commercial	1 M LiTFSI in TEGDME	Li	No (16.7% PTFE)	50 (μAh/cm ²)	Close to zero	Unknown	20 ^c
TiC-B powder	Commercial	1 M LiTFSI in TEGDME	Li	No (16.7% PTFE)	75 (μAh/cm ²)	2 (mAh)	Unknown	20 ^c
TiC NAs/CT	In-situ growth	0.5 M LiClO ₄ in DMSO	Li	Yes	29.3 (i.e., 0.1 mA/cm ²)	352 (1.2 mAh/cm ²)	125	This work
Ru-TiC NAs/CT	In-situ growth	0.5 M LiClO ₄ in DMSO	Li	Yes	29.3 (i.e., 0.1 mA/cm ²)	468 (1.6 mAh/cm ²)	270	This work
NiCo ₂ O ₄	Hydrothermal	1 M LiTFSI in TEGDME	Li	Yes	0.1 (mA/cm ²)	0.3 (mAh/cm ²)	1	21
Cr- NiCo ₂ O ₄	Hydrothermal	1 M LiTFSI in TEGDME	Li	Yes	0.1 (mA/cm ²)	1.2 (mAh/cm ²)	45	21
HPCM	Templating	1 M LiTFSI in TEGDME	Li	Yes	0.032 (mA/cm ²)	71 (μAh/cm ²)	100	22
HPCM/C	Templating	1 M LiTFSI in TEGDME	Li	Yes	0.032 (mA/cm ²)	39.4 (μAh/cm ²)	20	22
MCM	Templating	1 M LiTFSI in TEGDME	Li	Yes	0.032 (mA/cm ²)	19 (μAh/cm ²)	10	22
P ₄ O ₄	Computation	Unkown	Unkown	Unkown	Unkown	570.56	Unkown	23
RuO ₂ /CNT	ALD	1 M LiTFSI in TEGDME	Li	Yes	0.1 (mA/cm ²)	1.6 (mAh/cm ²)	80	24
GO-10mg	Hummers	1 M LiBF ₄ in NMP	Li	Yes	0.1 (mA/cm ²)	200	65	25
GO-30mg	Hummers	1 M LiBF ₄ in NMP	Li	Yes	0.1 (mA/cm ²)	400	85	25
GO-50mg	Hummers	1 M LiBF ₄ in NMP	Li	Yes	0.1 (mA/cm ²)	500	85	25
Co ₃ O ₄ /Carbon	Electrospin	1M LiCF ₃ SO ₃ /TEGDME	Li	Yes	500	760	20	26
Carbon	Electrospin	1M LiCF ₃ SO ₃ /TEGDME	Li	Yes	500	72	20	26
(RuO _x / TiN)	Deposition	1 M LiTFSI in TEGDME	Li	Yes	50	500	300	27
GO	Hummer's	1 M LiPF ₆ in TEGDME	Li	Yes	0.01 (mA/cm ²)	1150	≥10	28
MnO ₂ /Ni	Hydrothermal	1 M LiClO ₄ in PC/DEC	Li	Yes	0.1 (mA/cm ²)	0.93 (mAh/cm ²)	50	29
N doped carbon	Pyrolysis	1M LiCF ₃ SO ₃ /TEGDME	Li	Binder-free	0.1 (mA/cm ²)	100	61	30
Ru/RuO _x /ITO	Wet Chemical	0.5 M LiClO ₄ in DMSO	Li	No (5% CMC)	0.05 (mA/cm ²)	8 (mAh/cm ²)	60	31
m-TiN	Wet Chemical	1 M LiClO ₄ in TEGDME	Li	No (5% PVDF)	50	650	280	32
RuO ₂ /Ni	Sol-gel	1 M LiTFSI in TEGDME	Li	Yes	0.1 (mA/cm ²)	0.76 (mAh/cm ²)	75	33
Inverse opal C	Sol-gel	0.3M LiTFSI/PYR14TFSI	Li	Yes	0.085 (mA/cm ²)	27	Unkown	34

^a The discharge current density resulted in the discharge capacity in the following column.

^b The cycle number might result from a current density different from the discharge current density. We select the closet value to this work, if possible.

^c In ref. 20, Li₂O₂-loaded TiC-A and TiC-B were studied. The current density and capacity refer to charge current density and capacity.

In Table S2, we list the performance of other cathode materials published. Free standing (or binder-free) cathodes or non-carbonous cathodes are selected for comparison. Compared to the performance of carbonous cathodes, the specific capacity listed here is lower. This is reasonable, since carbon has much lower molecular weight and package density. From the table, the cathodes in this work provide high cycle number, which can be ascribed to the stability of TiC cathodes.

Theoretical mass of Li₂O₂ calculation

The theoretical amount of Li₂O₂ formed during discharge can be calculated by using

Faraday's Law that determines the theoretical capacity for Li₂O₂:

$$\rho^*_{Li_2O_2} = \frac{F \times Z_r}{M} = 1168.2 \text{ Ah/kg}_{Li_2O_2}$$

$$F = 96485 \text{ C/mol} = 26.8 \text{ Ah/mol}$$

$$Z_r = 2 \text{ electrons, unitless}$$

$$M = 45.881 \times 10^{-3} \text{ kg}_{NaO_2}/\text{mol}$$

The theoretical mass increase of NaO₂ is then as follows:

$$r_{Li_2O_2} = \frac{1}{\rho^*_{Li_2O_2}} = 8.56 \times 10^{-4} \text{ kg}_{NaO_2}/\text{Ah} = 0.856 \text{ mg/mAh}$$

In operando XRD measurement

The collected patterns from SR-PXD were converted to a plot of intensity vs. 2θ by Fit2D. All structural refinements of in situ data in this study were implemented by program FullProf. To quantify the amount of Li₂O₂ that was formed during the discharge and decomposed during the charge, a known amount of Si was introduced into the *in operando* cell, as shown in Figure S12. When the X-ray penetrated the cell, the diffraction from the Si and the discharge products (Li₂O₂) was detected simultaneously. In a Rietveld refinement software (Fullprof was applied in this study) the weight ratio between the detected Li₂O₂ and the Si can be obtained.

The efficiency of Li₂O₂ formation and decomposition was calculated by the following equation:

$$R_{Li_2O_2} = \frac{\Delta m_{Li_2O_2, E}}{\Delta m_{Li_2O_2, Cf}}$$

where $\Delta m_{Li_2O_2, E}$ and $\Delta m_{Li_2O_2, Cf}$ are the gain weight of Li_2O_2 detected by X-ray diffraction and the ideal amount of Li_2O_2 calculated given a $2 e^- / Li_2O_2$ process during cycle (0.856 mg Li_2O_2 per mAh would be expected), respectively.

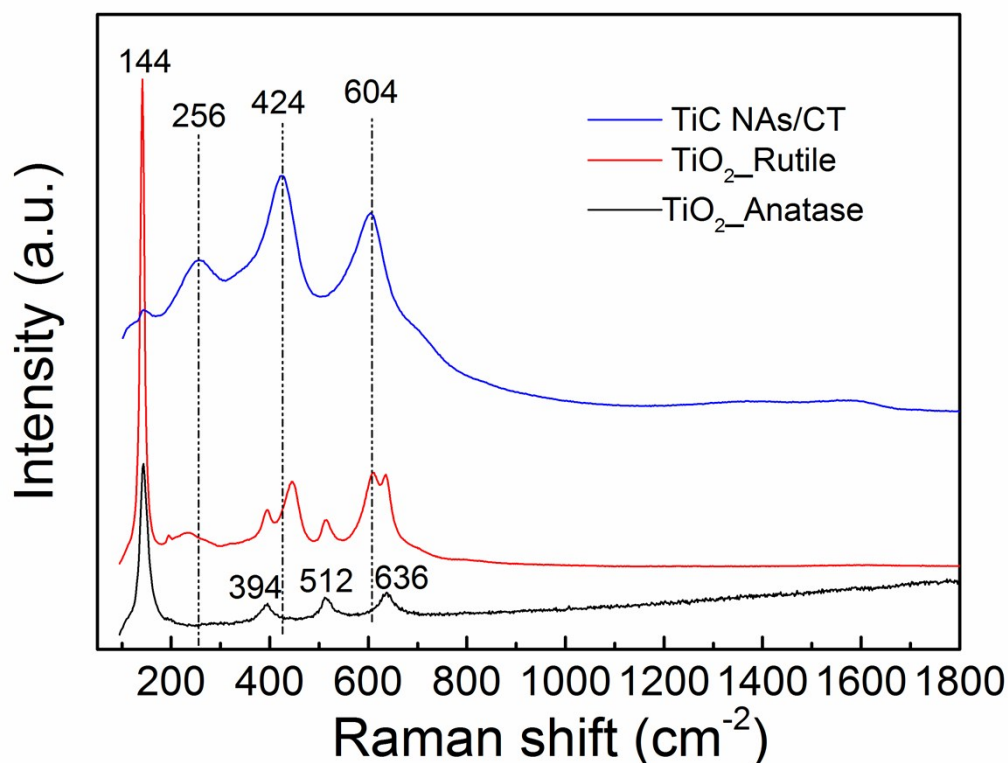


Figure S1. Raman spectra of the commercial anatase TiO_2 powder (< 25 nm, 99.7%, Aldrich chemistry), commercial rutile TiO_2 powder (< 100 nm, 99.5%, Aldrich chemistry) and the as prepared TiC NAs/CT.

The precursor for synthesis the TiC NAs/CT was the anatase TiO_2 powder. After 1250 °C of heating, the Raman peak of the anatase TiO_2 at 394, 512 and 636 cm^{-1} disappeared. However, the Raman peak at 144 cm^{-1} remained after the synthesis. This indicates that a small amount of rutile TiO_2 is exist. This result can be confirmed by XPS measurement, as shown in Figure 7.

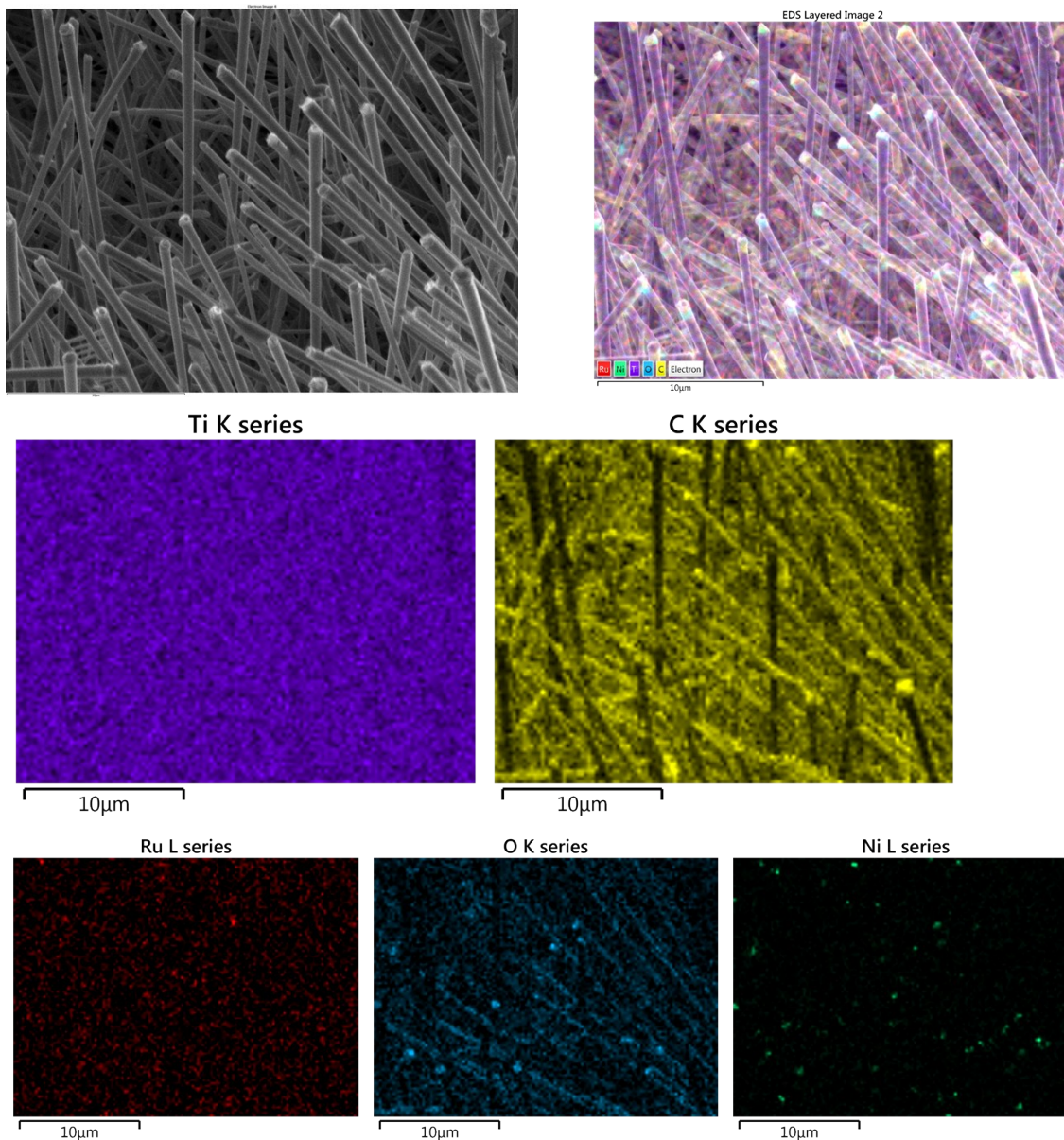


Figure S2. SEM image of the Ru-TiC NAs/CT with a Ni catalyst on the top, and the corresponding EDS mapping (with all captions above the corresponding images).

Figure S2 showed the elemental distribution in the Ru-TiC/C sample.

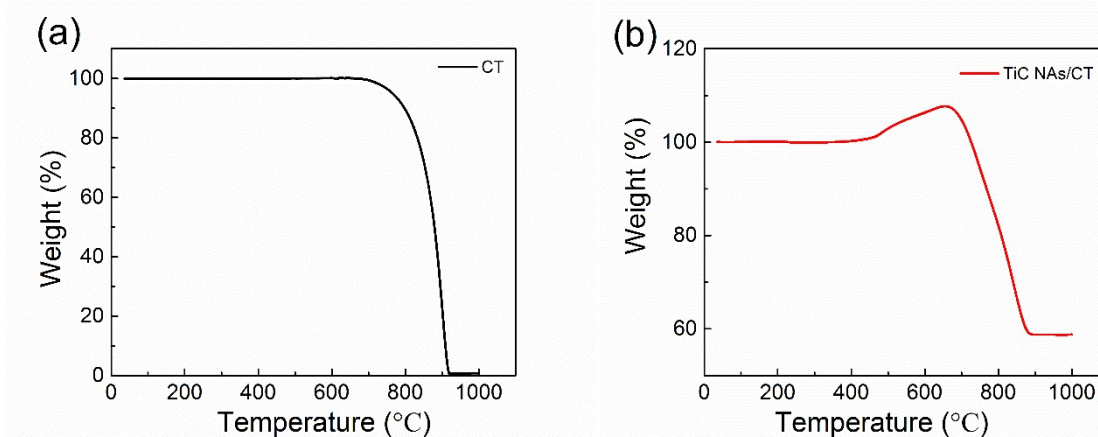


Figure S3. The TGA curves of (a) CT and (b) TiC NAs/CT under air atmosphere

Figure S3 showed the TGA results of the CT and TiC NAs/CT under air atmosphere. It can be seen that the oxidation of TiC started about 500 °C and the oxidation of carbon textile started after 700 °C. After 1000 °C oxidation in air, the TiC NAs/CT sample has reached its constant weight residual at 58.7%. The following equation displayed the oxidation process of TiC and the carbon in the air atmosphere:



Therefore, the weight fraction of TiC in the final synthesized TiC NAs/CT sample was calculated as following:

$$W_{\text{TiC}}(\text{wt}\%) = 100 \times \left(\frac{m \times M_{\text{TiC}}}{M_{\text{TiO}_2}} \right)$$

Where m is the weight percentage of TiO_2 after the TGA measurement. M_{TiC} and M_{TiO_2} are the molecular mass of TiC and TiO_2 , respectively. According to the TGA curve in Figure S3, the amount of TiC in the sample is calculated to be 44.0 %.

In addition, to confirm that all of the TiC in the sample has been fully oxidized to TiO_2 under environment during the TGA measurement, the same TiC NAs/CT sample was heated in the furnace at 1250 °C for 5h under air atmosphere.³⁵ The weight percentage of the residual oxides was about 58.2 %, which is very close to the TGA result.

Besides, the TGA results were further supported by ICP measurement as shown in Table S3.

Table S3. Summary of the ICP analysis

Sample	Ru wt%	Ti wt%
Ru-TiC NAs/CT	1.91	33.89

As shown in Table S3, the amount of Ti is 33.89 wt%, indicating the amount of TiC is 42.4 wt%.

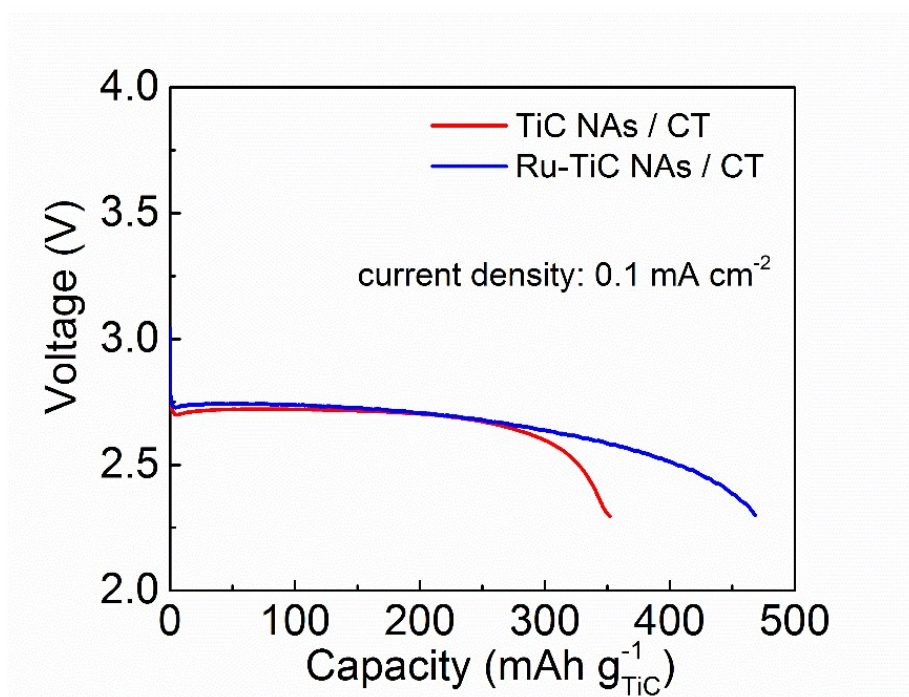


Figure S4. (a) Full discharge curve of Li-O₂ cells with the as-prepared TiC NAs/CT and Ru-TiC NAs/CT cathodes with a cut-off voltage at 2.3 V and a current density of 0.1 mA cm⁻² (29.3 mA g_{TiC}⁻¹, corresponding to 12.9 mAh g⁻¹ based on the total weight of cathode).

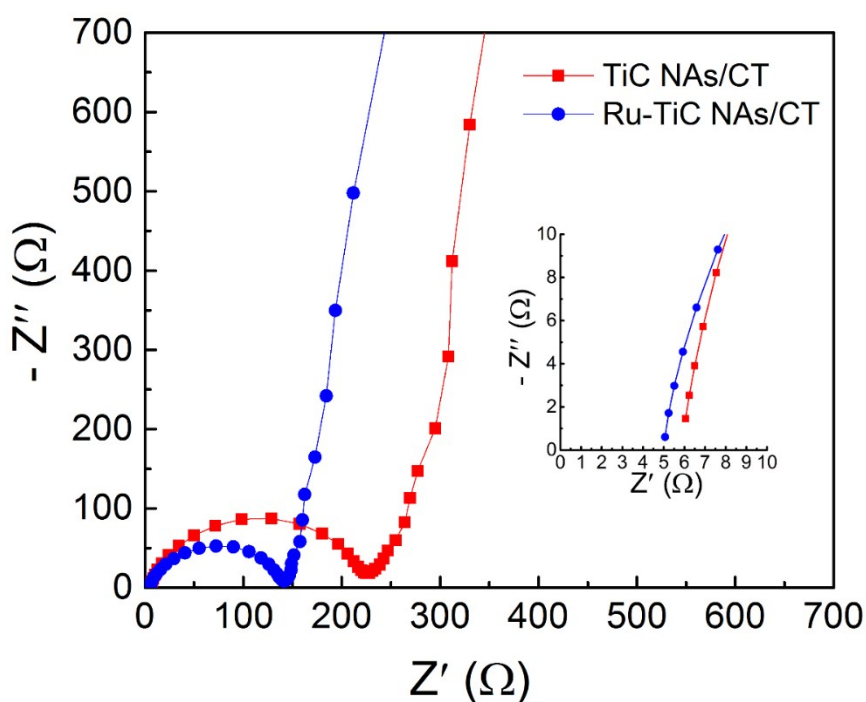


Figure S5. Nyquist plots for the corresponding TiC NAs/CT and Ru-TiC NAs/CT cathode in the Li-O₂ cells, the insert shows the magnification of the high frequency region.

The influence of Ru decoration on the TiC surface can be also revealed by comparing the EIS curves of the Ru-TiC NAs/CT and TiC NAs/CT electrodes. Figure S5 depicts Nyquist plots recorded for the cathodes in the cells. While both cells exhibited a similar solution resistance (R_s , i.e. the high frequency intercepts with the x-axes), the charge transfer resistance (R_{ct} , obtained from the diameters of the semicircles) is larger for the TiC NAs/CT cell. The R_s values for the TiC NAs/CT and Ru-TiC NAs/CT cells were found to be 6 Ω and 5 Ω , respectively. The resistance change along the cycling can be reflected by the voltage change in Figure 6c in the main text.

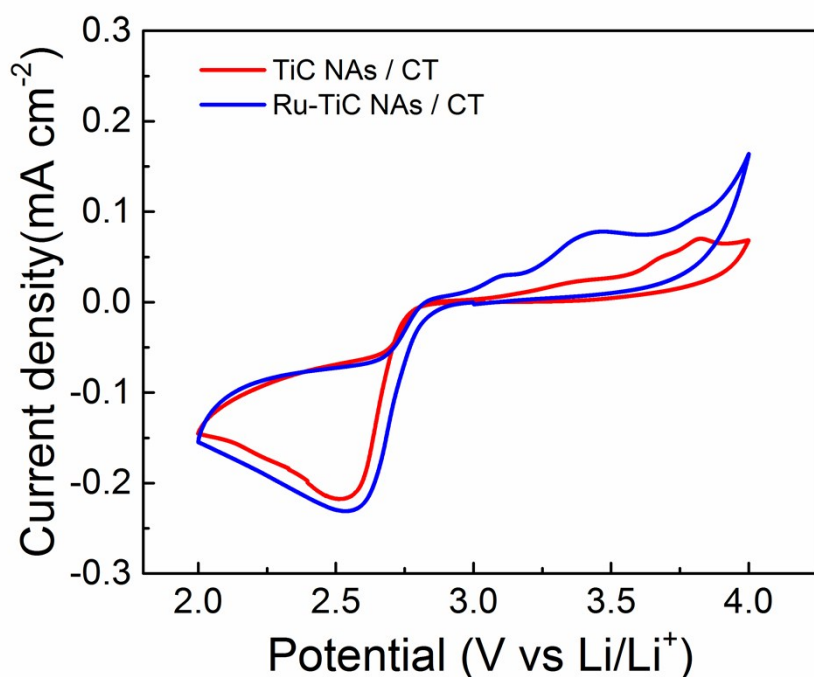


Figure S6. Cyclic voltammograms of the TiC NAs/CT and Ru-TiC NAs/CT cells at a scan rate of 0.05 mV s^{-1} .

To better understand the electrochemical characteristics of the cathodes during the ORR and OER process in Li-O₂ cells, cyclic voltammetry (CV) measurements were performed between 2.0 V to 4.0 V at a scanning rate of 0.05 mV s^{-1} . As shown in Figure S6, the ORR onset potential for TiC NAs/CT cathode is around 2.9 V (versus Li⁺/Li in the cathodic scan). Compared with TiC NAs/CT cathode, Ru-TiC NAs/CT exhibits a higher ORR onset potential shift, about 3.0 V, indicating a little lower ORR overpotential. In addition, the Ru-TiC NAs/CT cathode shows more apparent ORR and OER peaks and higher current density during the cathodic and anodic scans. These results indicate a higher catalytic activity of Ru-TiC NAs/CT, compared to TiC NAs/CT cathode.

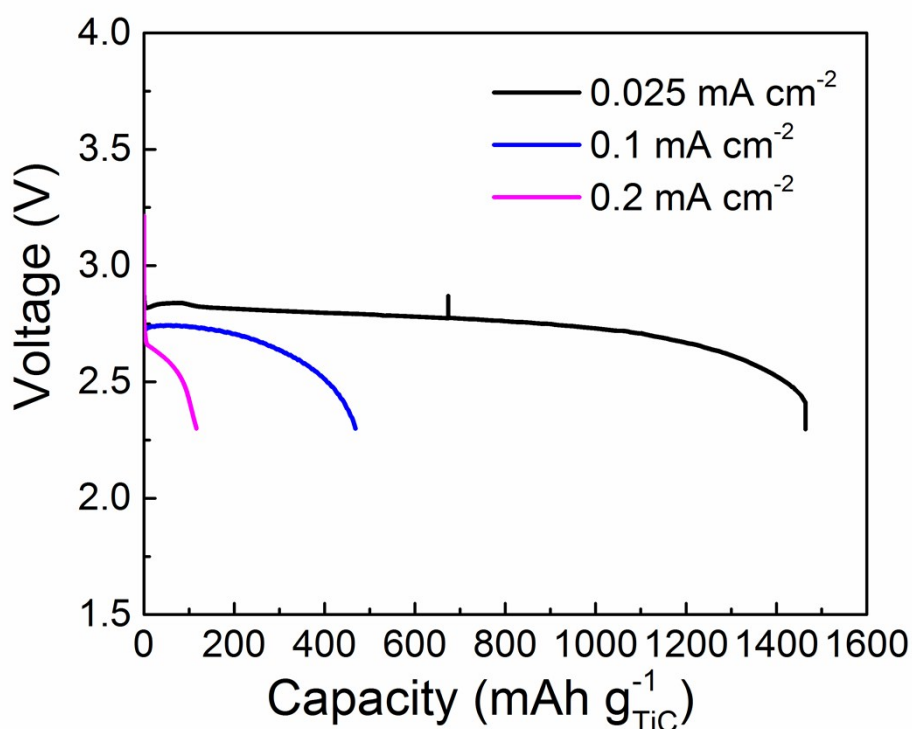


Figure S7. The rate performance of the Ru-TiC NAs/CT cells

It can be seen from Figure S7, the discharge capacity decreases with the increasing current density (by 4 times and 8 times).

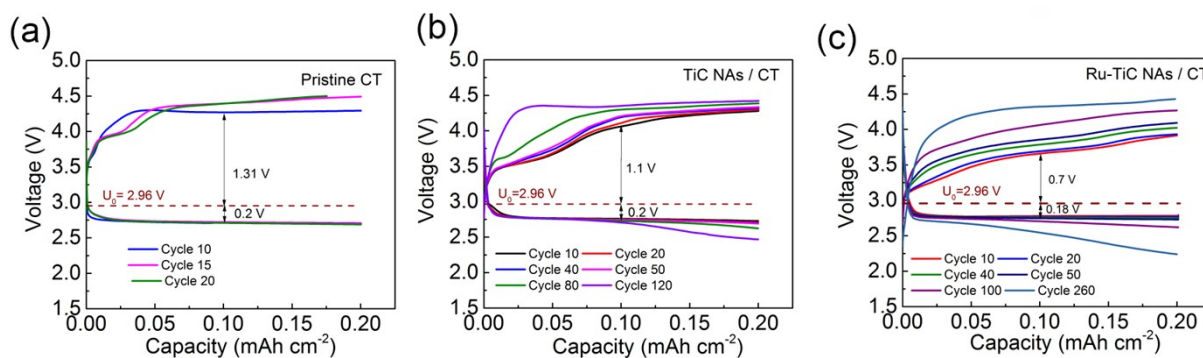


Figure S8. The selected galvanostatic discharge-charge curves of the cells with (a) pristine CT cathode, (b) TiC NAs/ CT cathode and (c) Ru-TiC NAs/ CT cathode at a current density of 0.05 mA cm^{-2} .

At a current density of 0.05 mA cm^{-2} , the cycleability of the cell with pristine CT cathode was rather unsatisfactory (Figure S8a). With a cut off voltages of 2.0 V and 4.5 V vs. Li^+/Li and a

limited capacity of 0.2 mAh cm^{-2} , the battery was only stable up to 15 cycles with a large overpotential up to 1.51 V at the 10th cycle. Introducing TiC on the carbon surface improved the cycleability, and the overpotential of the cell was reduced (Figure S8b). As shown in Figure S8c, the cycleability and overpotential have been further improved by loading Ru on the surface of the TiC.

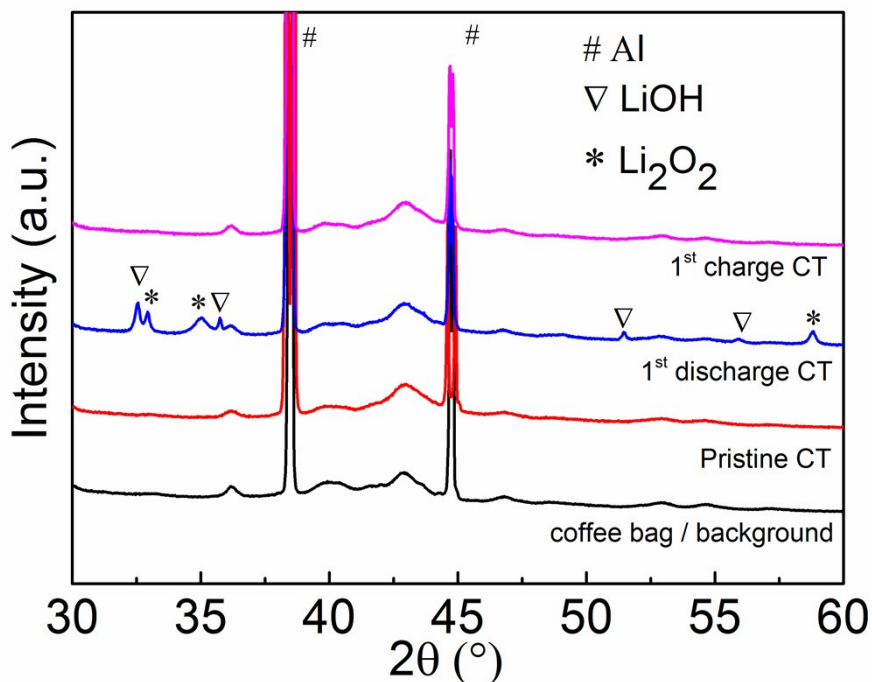


Figure S9. XRD patterns of pristine, discharged and charged cathodes of CT

To confirm that Li_2O_2 was reversibly formed and decomposed, ex-situ XRD was carried out for the cell with CT cathode. Compared to the pristine cathode, the discharge cathode shows new diffraction peaks at 32.9° , 35.0° and 58.8° (Figure S9), which can be assigned to Li_2O_2 (100), (101) and (110), respectively. However, without the protection of TiC, LiOH was detected from CT cathode after discharge, which indicates the decomposition of DMSO electrolyte. This gives further evidence of the importance of carbon cathode protection. No Li_2O_2 peaks were observed for the cathode after the first cycle, which means that the Li_2O_2 and LiOH formed during discharge were decomposed during the charge process.

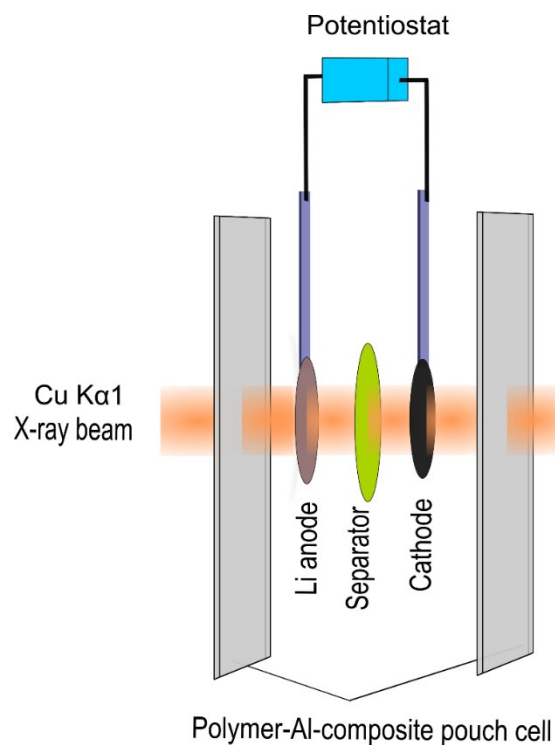


Figure S10. Schematic view of the Li-O₂ cell for in-house *in operando* XRD study

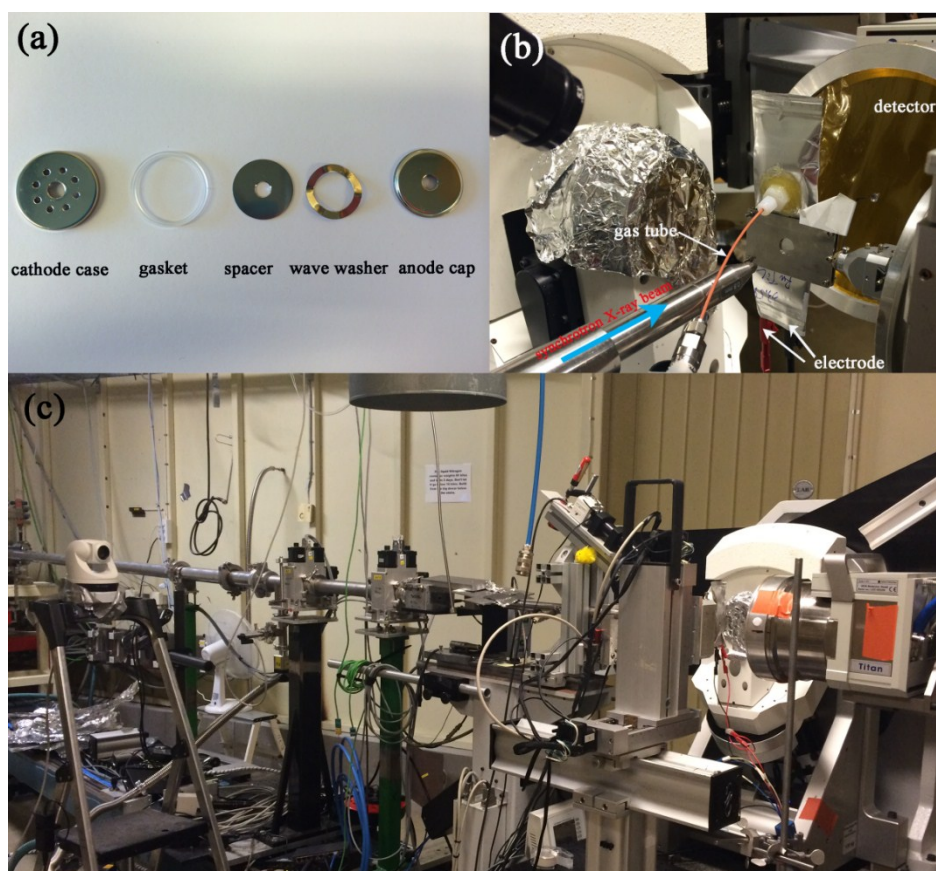


Figure S11. Photos of (a) components of an *in operando* Li-O₂ cell, (b) and (c) an assembled Li-O₂ cell mounted on synchrotron beamline I711, Lund, Sweden.

***In operando* Li-O₂ cell design**

Operando XRD measurements were performed using a specifically homemade Li-O₂ cell, which allowed X-ray to penetrate the cell, being measured in transmission mode during battery cycling. The cell hardware contained a standard coin cell (size 2025, Hohsen Corp) with a 4 mm diameter hole at the center on each side (for X-ray passing through), eight 1.5 mm diameter holes at 5 mm distance from the center on the case of the cathode side (for oxygen diffusion), and a 4 mm diameter hole at the center of spacer (for X-ray beam to pass through). The as-prepared electrode served as the cathode (13 mm diameter), double-layer Solupor as separator (17 mm diameter) soaked with excessive electrolyte (1 M LiClO₄ in DMSO), and a lithium foil disc (15 mm in diameter) as the anode being placed inside the coin cell case. A spacer, a wave washer and a lid of the cell were placed before crimping the cell. The hole in the lid was sealed by a thin layer of Si film with Kapton, serving as a reference for XRD quantification and protecting Li metal from oxidation. The assembled coin cell was then sealed in a “coffee bag” (aluminum pouch cell) that was connected to a gas pipe with a quick connector, shown in Figure S12.

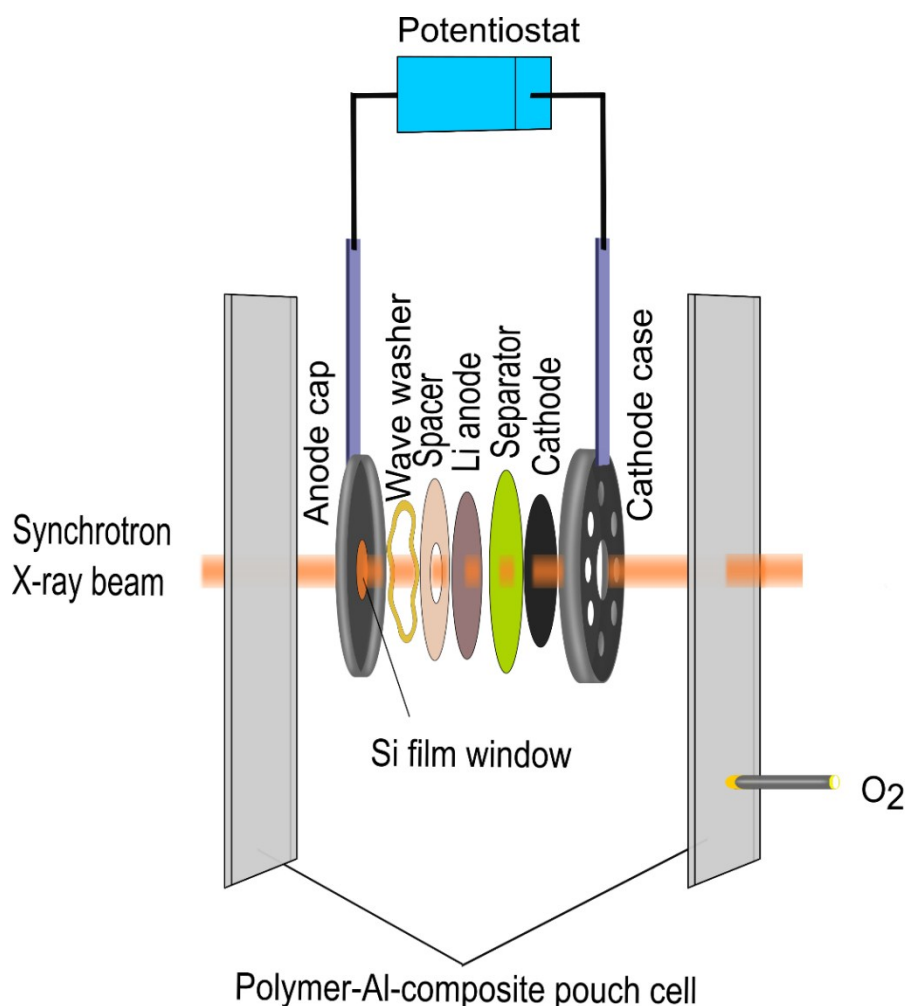


Figure S12. Schematic view of the Li-O₂ cell for *in operando* SR-PXD study

Reference

1. L. Johnson, C. Li, Z. Liu, Y. Chen, S. A. Freunberger, P. C. Ashok, B. B. Praveen, K. Dholakia, J. M. Tarascon and P. G. Bruce, *Nat. Chem.*, 2014, **6**, 1091-1099.
2. J. P. Vivek, N. G. Berry, J. Zou, R. J. Nichols and L. J. Hardwick, *J. Phys. Chem. C*, 2017, **121**, 19657-19667.
3. B. D. McCloskey, A. Speidel, R. Scheffler, D. C. Miller, V. Viswanathan, J. S. Hummelshoj, J. K. Nørskov and A. C. Luntz, *J. Phys. Chem. Lett.*, 2012, **3**, 997-1001.
4. B. D. McCloskey, R. Scheffler, A. Speidel, D. S. Bethune, R. M. Shelby and A. C. Luntz, *J. Am. Chem. Soc.*, 2011, **133**, 18038-18041.
5. Y. C. Lu, E. J. Crumlin, G. M. Veith, J. R. Harding, E. Mutoro, L. Baggetto, N. J. Dudney, Z. Liu and Y. Shao-Horn, *Sci Rep*, 2012, **2**, 715.
6. H. Zheng, D. Xiao, X. Li, Y. Liu, Y. Wu, J. Wang, K. Jiang, C. Chen, L. Gu, X. Wei, Y. S. Hu, Q. Chen and H. Li, *Nano Lett.*, 2014, **14**, 4245-4249.
7. L. Zhong, R. R. Mitchell, Y. Liu, B. M. Gallant, C. V. Thompson, J. Y. Huang, S. X. Mao and Y. Shao-Horn, *Nano Lett.*, 2013, **13**, 2209-2214.
8. R. Wen, M. Hong and H. R. Byon, *J. Am. Chem. Soc.*, 2013, **135**, 10870-10876.
9. H. Lim, E. Yilmaz and H. R. Byon, *J. Phys. Chem. Lett.*, 2012, **3**, 3210-3215.
10. S. Ganapathy, B. D. Adams, G. Stenou, M. S. Anastasaki, K. Goubitz, X. F. Miao, L. F. Nazar and M. Wagemaker, *J. Am. Chem. Soc.*, 2014, **136**, 16335-16344.
11. Z. Yang, L. Trahey, Y. Ren, M. K. Y. Chan, C. Lin, J. Okasinski and M. M. Thackeray, *J. Mater. Chem. A*, 2015, **3**, 7389-7398.
12. M. M. Storm, R. E. Johnsen, R. Younesi and P. Norby, *J. Mater. Chem. A*, 2015, **3**, 3113-3119.
13. J. L. Shui, J. S. Okasinski, P. Kenesei, H. A. Dobbs, D. Zhao, J. D. Almer and D. J. Liu, *Nat. Commun.*, 2013, **4**, 2255.
14. K. R. Ryan, L. Trahey, J. S. Okasinski, A. K. Burrell and B. J. Ingram, *J. Mater. Chem. A*, 2013, **1**, 6915-6919.
15. S. Ganapathy, J. R. Heringa, M. S. Anastasaki, B. D. Adams, M. v. Hulzen, S. Basak, Z. Li, J. P. Wright, L. F. Nazar, N. H. v. Dijk and M. Wagemaker, *J. Phys. Chem. Lett.*, 2016, **7**, 3388-3394.
16. J. L. Shui, J. S. Okasinski, C. Chen, J. D. Almer and D. J. Liu, *ChemSusChem*, 2014, **7**, 543-548.
17. J. L. Shui, J. S. Okasinski, D. Zhao, J. D. Almer and D. J. Liu, *ChemSusChem*, 2012, **5**, 2421-2426.
18. C. Liu, W. R. Brant, R. Younesi, Y. Dong, K. Edström, T. Gustafsson and J. Zhu, *ChemSusChem*, 2017, **10**, 1592-1599.
19. M. M. Ottakam Thotiyl, S. A. Freunberger, Z. Peng, Y. Chen, Z. Liu and P. G. Bruce, *Nat. Mater.*, 2013, **12**, 1050-1056.
20. B. D. Adams, R. Black, C. Radtke, Z. Williams, B. L. Mehdi, N. D. Browning and L. F. Nazar, *ACS Nano*, 2014, **8**, 12483-12493.
21. D. Giacco, A. G. Marrani, S. Brutti. *Mater. Lett.*, 2018, **224**, 113-117.
22. S. Xu, X. Liang, Z. Ren, K. Wang, J. Chen. *Angew. Chem. Int. Ed.*, 2018, **57**, 6825-6829.
23. Y. Li, F. Ma, L. Wang. *J. Mater. Chem. A*, 2018, **6**, 7815.
24. H. Shin, G. W. Seo, K. Kwon, K. Jung, S. I. Lee, E. Choi, H. Kim, J. Hwang. *Appl Mater.*, 2018, **6**, 047702.
25. S. Özcan, T. Cetinkaya, M. Tokur, H. Algul, M. O. Guler, H. Akbulut, *Intern. J. Hydro. Energy*, 2016, **41**, 9796-9802.
26. M. J. Song, I. T. Kim, Y. B. Kim, M. W. Shin. *Electrochim. Acta*, 2015. **182**. 289-296.
27. Y. Chang, S. Dong, Y. Ju, D. Xiao, X. Zhou, L. Zhang, X. Chen, C. Shang, L. Gu, Z. Peng, G. Cui. *Adv. Sci.* 2015, **2**, 1500092.

28. T. Cetinkaya, S. Ozcan, M. Uysal, M. O. Guler, H. Akbulut. *J. Power Source*. 2014, 267, 140-147.
29. Y. Yu, B. Zhang, Z. Xu, Y. He, J. Kim. *Solid State Ionics*. 2013, 262, 197-201.
30. S. Jing, M. Zhang, H. Liang, B. Shen, S. Yin, X. Yang. *J. Mater. Sci.*, 2018, 53, 4395-4405.
31. S. Vankova, C. Francia, J. Amici, J. Zeng, S. Bodoardo, N. Penazzi, G. Collins, H. Geaney, C. O'Dwyer. *ChemSusChem*, 2017, 10, 575-586.
32. B. G. Kim, C. Jo, J. Shin, Y. Mun, J. Lee, J. W. Choi. *ACS Nano*, 2017, 11, 1736-1746.
33. C. Liu, C. Li, K. Ahmed, W. Wang, I. Lee, F. Zaera, C. S. Ozkan, M. Ozkan. *RSC Adv.*, 2016, 6, 81712-81718.
34. M. Olivares-Marin, P. Palomino, J. M. Amarilla, E. Enciso, D. Tonti. *J. Mater. Chem. A*, 2013, 1, 14270-14279.
35. R. F. Voitovich and É. A. Pugach, *Soviet Powder Metallurgy and Metal Ceramics*, 1972, 11, 132-136.